

High-resolution imaging of magnetic fields of banknote anti-counterfeiting strip using fiber diamond probe

Xu-Tong Zhao(赵旭彤), Fei-Yue He(何飞越), Ya-Wen Xue(薛雅文), Wen-Hao Ma(马文豪), Xiao-Han Yin(殷筱晗), Sheng-Kai Xia(夏圣开), Ming-Jing Zeng(曾明菁), and Guan-Xiang Du(杜关祥)

Citation: Chin. Phys. B, 2024, 33 (**4**): 048502. DOI: 10.1088/1674-1056/ad1b44
Journal homepage: http://cpb.iphy.ac.cn; http://iopscience.iop.org/cpb

What follows is a list of articles you may be interested in

Increasing linear flux range of SQUID amplifier using self-feedback effect

Ying-Yu Chen(陈滢宇), Chao-Qun Wang(王超群), Yuan-Xing Xu(徐元星), Yue Zhao(赵越), Li-Liang Ying(应利良), Hang-Xing Xie(谢颃星), Bo Gao(高波), and Zhen Wang(王镇)

Chin. Phys. B, 2023, 32 (**11**): 118501. DOI: 10.1088/1674-1056/acd8ac

A non-quasi-static model for nanowire gate-all-around tunneling field-effect transistors

Bin Lu(芦宾), Xin Ma(马鑫), Dawei Wang(王大为), Guoqiang Chai(柴国强),Linpeng Dong(董林鹏), and Yuanhao Miao(苗渊浩)

Chin. Phys. B, 2023, 32 (**6**): 068501. DOI: 10.1088/1674-1056/acbe32

A 4H-SiC trench IGBT with controllable hole-extracting path for low loss

Lijuan Wu(吴丽娟), Heng Liu(刘恒), Xuanting Song(宋宣廷), Xing Chen(陈星), Jinsheng Zeng(曾金胜), Tao Qiu(邱滔), and Banghui Zhang(张帮会)

Chin. Phys. B, 2023, 32 (**4**): 048503. DOI: 10.1088/1674-1056/ac8722

Improvement on short-circuit ability of SiC super-junction MOSFET with partially widened pillar structure

Xinxin Zuo(左欣欣), Jiang Lu(陆江), Xiaoli Tian(田晓丽), Yun Bai(白云), Guodong Cheng(成国栋), Hong Chen(陈宏), Yidan Tang(汤益丹), Chengyue Yang(杨成樾), and Xinyu Liu(刘新宇)

Chin. Phys. B, 2022, 31 (**9**): 098502. DOI: 10.1088/1674-1056/ac6159

Modeling and numerical simulation of electrical and optical characteristics of a quantum dot light-emitting diode based on the hopping mobility model: Influence of quantum dot concentration

Pezhman Sheykholeslami-Nasab, Mahdi Davoudi-Darareh, and Mohammad Hassan Yousefi

Chin. Phys. B, 2022, 31 (**6**): 068504. DOI: 10.1088/1674-1056/ac364b

---

High-resolution imaging of magnetic fields of banknote anti-counterfeiting strip using fiber diamond probe

Xu-Tong Zhao(赵旭彤)[1], Fei-Yue He(何飞越)[1], Ya-Wen Xue(薛雅文)[2], Wen-Hao Ma(马文豪)[1], Xiao-Han Yin(殷筱晗)[1], Sheng-Kai Xia(夏圣开)[3], Ming-Jing Zeng(曾明菁)[4], and Guan-Xiang Du(杜关祥)[1,†]

[1] *College of Telecommunications and Information Engineering, Nanjing University of Posts and Telecommunications, Nanjing* 210003, *China*
[2] *College of Science, Nanjing University of Posts and Telecommunications, Nanjing* 210003, *China*
[3] *School of Computer Science, Nanjing University of Posts and Telecommunications, Nanjing* 210023, *China*
[4] *Bell Honors School, Nanjing University of Posts and Telecommunications, Nanjing* 210023, *China*

(Received 5 October 2023; revised manuscript received 20 November 2023; accepted manuscript online 5 January 2024)

Counterfeiting of modern banknotes poses a significant challenge, prompting the use of various preventive measures. One such measure is the magnetic anti-counterfeiting strip. However, due to its inherent weak magnetic properties, visualizing its magnetic distribution has been a longstanding challenge. In this work, we introduce an innovative method by using a fiber optic diamond probe, a highly sensitive quantum sensor designed specifically for detecting extremely weak magnetic fields. We employ this probe to achieve high-resolution imaging of the magnetic fields associated with the RMB 50 denomination anti-counterfeiting strip. Additionally, we conduct computer simulations by using COMSOL Multiphysics software to deduce the potential geometric characteristics and material composition of the magnetic region within the anti-counterfeiting strip. The findings and method presented in this study hold broader significance, extending the RMB 50 denomination to various denominations of the Chinese currency and other items that employ magnetic anti-counterfeiting strips. These advances have the potential to significantly improve and promote security measures in order to prevent the banknotes from being counterfeited.

Keywords: banknote anti-counterfeiting strip, nitrogen–vacancy (NV) centers, magnetic field imaging, numerical simulation

PACS: 85.75.Ss **DOI:** 10.1088/1674-1056/ad1b44

1. Introduction

Various methods are employed for banknote anti-counterfeiting, including watermarks, color-changing inks, and anti-counterfeiting strips. Among these methods, the anti-counterfeiting strip has proven to be one of the most reliable measures. Recent advancements in science, technology, and manufacturing have enabled the integrating of special substances into these strips, creating a predetermined distribution of magnetic signals, thus enhancing banknote security. By keeping the composition of these magnetic signal-generating substances and their confidential geometric structure undisclosed, banknote security is significantly improved.

Currently, several methods are used to detect the magnetic regions in anti-counterfeiting strips on banknotes. These established methods predominantly rely on the visualization of electrical signals derived from magnetic signals.[1] However, this process involves multiple stages of signal amplification and shaping by specialized chips. Despite the fact that the resulting electrical signals have regular patterns, they lack detailed magnetic field information. Consequently, these methods can only determine the presence of a magnetic field in a specific area, but they do not provide accurate measurements of its magnitude or even an order of magnitude. Therefore, it is relatively easy to blur the boundary between genuine banknotes and counterfeit banknotes by duplicating the electrical signals that generate detection results similar to those of anti-counterfeiting tape. Hence, in view of these limitations, there is an urgent need for high-resolution visualization and imaging technology of magnetic signals to ensure that the detection results retain the magnetic distribution information within the security line to a maximum extent.

In the field of magnetic imaging, several direct techniques are available for sample testing, these including diverse methodologies, each with its own advantages and disadvantages. Notable among these techniques, the superconducting quantum interference device (SQUID),[2] the magneto-optical Kerr microscope (MOKE),[3] the magnetic force microscope (MFM),[4] and the scanning magneto-impedance (MI) magnetic microscope.[5] All rely on their distinct magnetic measurement principles, thus making them suitable to specific applications.

It is found that some of these techniques are effective in imaging the magnetic field distribution in banknotes.[5] However, due to the need for complex experimental equipment and strict environmental conditions (for example, extremely low temperatures), their wide applications are hindered.

In contrast, the diamond nitrogen–vacancy (NV) center presents an innovative and promising solution. This all-solid-

†Corresponding author. E-mail: duguanxiang@njupt.edu.cn
© 2024 Chinese Physical Society and IOP Publishing Ltd

state quantum platform exhibits remarkable spin-quantum properties[6] and improves several advantageous characteristics. These include compatibility with room temperature, extended coherence time, ease of polarization manipulation, and capabilities for spin state readout.[7] Furthermore, the diamond NV center displays the sensitivity to a wide range of physical quantities, including magnetic fields, temperature, electric fields, and stress.

In practice, it is found that the diamond NV centers possess diverse applications as sensors. They can be used for detecting temperature fields, electric fields, and stress fields, as well as responding to various magnetic signals, including stray fields[8,9] and alternating magnetic fields.[10–12] This versatility makes the diamond NV centers a promising way to promote the magnetic imaging technologies in a more convenient and multifunctional way.

In the field of magnetic imaging, since the pioneering work of successfully imaging stray magnetic fields with dense NV layer in 2008, diamond NV centers have shown great potential in a wide range of research fields.[13] Over the years, experimental devices and measurement techniques have been developed, the diamond NV centers have become an indispensable tool for magnetic field imaging in diverse areas of research. These areas include paleomagnetic studies,[14,15] biological magnetic detection,[16,17] solid-state matter magnetism,[18] and microelectronic magnetic imaging.[19,20] The application of NV centers in magnetic imaging highlights a crucial research direction aiming at addressing specific challenges in various fields.

This paper introduces a novel approach, *i.e.*, a fiber optic diamond probe features a micron-sized diamond as its sensing core, to conduct scanning imaging of the magnetic field generated by banknote anti-counterfeiting strips. This innovative technique can directly image the magnetic field produced by these strips with high resolution. Additionally, the COMSOL Multiphysics software is used to simulate and deduce the possible microstructure and material composition in the magnetic field generation region of the anti-counterfeiting strip based on the acquired magnetic field distribution and intensity information obtained through the scanning imaging process.

2. Experimental principle

2.1. Diamond NV center magnetic sensing principle

The diamond NV center is a luminescent point defect found in diamond crystal. It occurs when a carbon atom in the diamond lattice is replaced by a nitrogen atom and is combined with an adjacent vacancy, as depicted in Fig. 1(a). Diamond NV center has a C_{3v} symmetry, and the symmetry axis is the crystal axis where the nitrogen vacancy is located. The crystal axis is also known as the NV axis with four different directions. As shown in Fig. 1(b), the ground state configuration of an NV center is spin triplet state $^3A_2$[21] with $m_s = 0$ and $m_s = \pm 1$, respectively. $m_s = \pm 1$ is in the degenerate state when there is no external field, and there is a natural zero-field splitting between $m_s = 0$ and $m_s = \pm 1$ with the zero-field splitting parameter $D = 2.87$ GHz. When the NV center is irradiated by a laser of 532 nm, if the NV center is in the ground state $m_s = 0$, it will jump to the excited state $m_s = 0$ (as denoted by the solid green line in Fig. 1(b)), then return to the ground state $m_s = 0$ and release red fluorescence after a while (as indicated by the solid red line in Fig. 1(b)); If the NV center is in the ground state $m_s = \pm 1$, it will jump to the excited state $m_s = \pm 1$ (as represented by the green dotted line in Fig. 1(b)), then it has a possibility to go back to the ground state $m_s = 0$ after inter-system crossing (ISC) over $^1A_1$ and ^1E, in which process releases a small amount of red fluorescence[22] (as shown by the orange dotted line in Fig. 1(b)). Therefore, a period of irradiation with a 532-nm laser can make most of the NV centers return to the ground state $m_s = 0$, which is the process of NV center polarization.

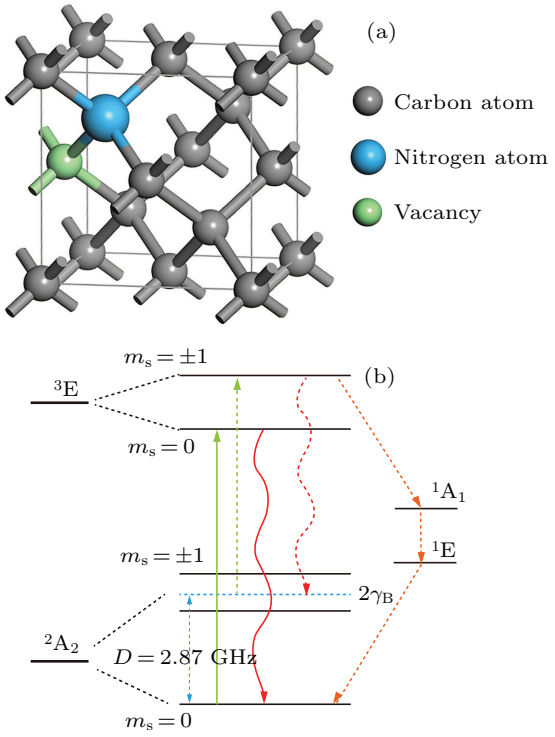


Fig. 1. (a) Diamond NV center structure and (b) diamond NV center energy level diagram.

Under the action of the external magnetic field, the ground state $m_s = \pm 1$ splits into $m_s = +1$ and $m_s = -1$ due to the Zeeman effect, and the energy gap is proportional to the magnitude of the external magnetic field.[23] We can use optical detection magnetic resonance (ODMR)[24] to detect the transition from $m_s = 0$ to $m_s = +1$ and $m_s = -1$ and measure the corresponding resonance frequencies $f_{i\pm}$, where the subscript i is used to distinguish the four axes, so eight peaks will be obtained to form the ODMR spectrum. For the determined axes, the applied magnetic field and the resonance frequencies

$f_{i\pm}$ are related by[23]

$$B_i = (f_{i+} - f_{i-})/(2\gamma_{\mathrm{NV}}), \tag{1}$$

where the γ_{NV} is the gyromagnetic ratio, which is about 2.8 MHz/Gs (1 Gs = 10^{-4} T). According to Eq. (1), the resonance frequencies change with the external magnetic field, and so do the ODMR peaks, for which the magnetic field strength can be calculated according to the offset of the peaks.

2.2. Experimental system

The magnetic field scanning imaging system consists of four main components: optical module, synchronous control module, data processing module, and scanning module, as illustrated in Fig. 2. Additionally, an N52 permanent magnet is located near the diamond to provide a bias magnetic field.

The optical module comprises two essential parts: laser excitation and fluorescence collection. A 532-nm laser is directed onto a long-pass dichroic mirror placed at a 45° angle. As the laser wavelength is smaller than the starting wavelength of the long-pass dichroic mirror, it reflects at a 90° angle towards objective 1. The laser is then focused by objective 1 and irradiated onto the fiber adapter, where it is coupled into the fiber to excite the diamond NV center at the fiber tip. The resulting red fluorescence emitted by the NV center is collected through an optical fiber. The fluorescence wavelength is in a range of approximately 600 nm–800 nm, exceeds the starting wavelength of the long-pass dichroic mirror. Consequently, it passes straight through the dichroic mirror, and a long-pass filter with a starting wavelength of 600 nm is employed to filter out any residual green light. Since the avalanche photo diode (APD) has a small photosensitive area (1 mm in diameter), objective 2 is utilized to focus the filtered fluorescence onto the APD's photosensitive area. The APD converts the fluorescent signals into electrical signals.[25] Prior to the experiment, meticulous adjustments were made to optimize each component of the optical module, ensuring maximal collection of the fluorescence signal by the APD.

The synchronous control module of the system comprises a pulse generator and a microwave source (not shown in Fig. 2). The microwave generated by the microwave source (Anapico-APSYN420, operating in a frequency range from 10 MHz to 20 GHz) is directed towards the diamond NV center via a multi-turn annular coil. This setup enables the controlling of the spin state of NV center. The pulse generator (Swabian Instrument Pulse Streamer 8/2) generates three TTL signals. The first signal serves as the laser pulse control, the second one is used for microwave pulse modulation, and the third signal is utilized for modulating the subcarrier pulse. Further details regarding the specific pulse settings will be described later.

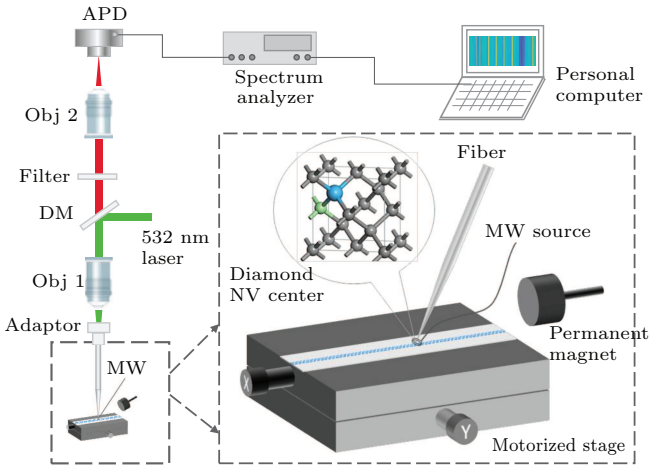


Fig. 2. The block diagram of banknote magnetic anti-counterfeiting strip scan experiment.

The data processing module primarily consists of a spectrum analyzer and LabVIEW program. The spectrum analyzer continuously measures the strength of the electrical signal converted from the APD at a specific frequency. The LabVIEW program enables the setting of experimental parameters (e.g., laser switching time, microwave switching time, scanning area of the displacement table, scanning step length) and facilitates the processing, display, and storage of experimental data.

The scanning module consists of an electric displacement table and a fiber optic diamond probe.[26,27] The electric displacement table fixes the measured sample and can perform controlled stepwise motion in the XY plane. The fiber optic diamond probe serves as the sensing core of the magnetic field scanning imaging system. The fiber tip (OM2 50 μm/125 μm) is tapered by using the thermal stretching method, resulting in a cone length of approximately 800 μm. A diamond particle with a diameter of about 20 μm is affixed to the tapered fiber tip by using UV glue.

3. Experimental results

3.1. Magnetic field scanning results

Experimental pulse sequences, including the timing arrangements of both laser signal and microwave signal. During the experiment, when the laser is at a low level, the microwave signal is at a high level. At this point, the NV center undergoes spin state changing under the influence of the microwave. Subsequently, when the laser is at a high level, the microwave signal is at a low level. The fluorescence signal changes caused by the spin state variations of the NV center are then read by using the laser.

Prior to the ODMR experiment, we configure the three TTL signals as illustrated in Fig. 3(a). The first TTL signal is used to modulate the laser, and its high level duration is 500 ns and a low level duration is 500 ns. It operates at a frequency of 1 MHz. The microwave signal has a high level duration of

450 ns and a low level duration of 50 ns in the time window when the laser is turned off. During the time window of turning on the laser, the microwave signal is kept at a low level, and the frequency of the second TTL signal is also kept at 1 MHz. The third TTL signal generates a 1-kHz pulse, serving as a subcarrier to modulate the output of the microwave source. It has a high level duration of 500 μs and a low level duration of 500 μs. In addition to the small-period modulation of 1 MHz, the microwave signal also undergoes a large-period modulation of 1 kHz as shown in Fig. 3(a) with $N = 500$.

The fluorescence signal, resulting from the alternating action of the laser and microwave modulated by the first TTL signal and second TTL signal, is referred to as the main frequency signal V_c. In the frequency domain, this signal is located at a frequency of 1 MHz. Additionally, after being modulated by the third TTL signal, the fluorescence signal in which the microwave is turned off in the second half cycle minus the fluorescence signal in which the microwave is turned on in the first half cycle, is known as the sideband signal V_s. In the frequency domain, the sideband signal is located at 1.001 MHz.

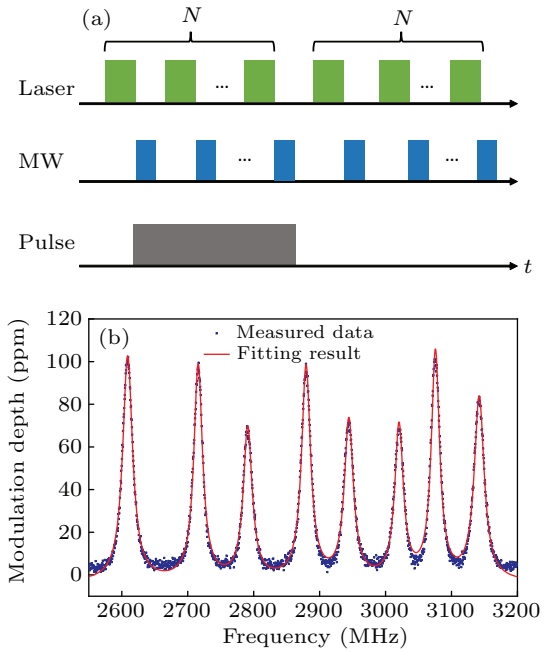


Fig. 3. (a) Laser, microwave, subcarrier pulse sequence. (b) Eight-peak ODMR spectrum.

The sideband signal V_s is obtained by subtracting the optical shot noise, laser noise, and APD noise from the signal. Since it is predominantly influenced by the effect of the microwave, the sideband signal provides a significant improvement in the signal-to-noise ratio. When the frequency of the microwave resonates with the energy level of the NV center, the main frequency signal V_c decreases, while the sideband signal V_s increases. The ratio of V_s to V_c, known as the modulation depth, is defined as an indicator of this effect.

By applying different microwave frequencies, the spectrum analyzer reads and captures both the main frequency signal and the sideband signal. This process ultimately yields ODMR spectrum, which consists of eight peaks, as illustrated in Fig. 3(b). The experimental data are depicted by the blue points, while the red curves represent the fitting results obtained by using the Lorentz function as follows:

$$S(Awf_0) = \frac{Aw^2}{(f-f_0)^2+w^2}, \tag{2}$$

where S represents the detected fluorescence intensity signal, A is the maximum fluorescence intensity signal for each spectral peak, w is 1/4 of the width of the resonance peak, f is the frequency of the microwave, and f_0 is the center frequency of the spectral peak.

From Eq. (1), the magnetic field can be calculated by analyzing the position changes of the ODMR peaks. By recording the variations in the ODMR peaks at each scanning point, we can obtain an image depicting the distribution of the magnetic field in the tested sample. It is important to note that we focus on studying the trend of the magnetic field distribution rather than obtaining precise numerical values. Therefore, we utilize the frequency change of a single peak to calculate the magnetic field, and the magnetic field obtained represents the projected component of the total magnetic field on an NV axis.

To validate the accuracy of our imaging method of reflecting the magnetic field distribution, we perform a scan and imaging of the magnetic field generated around an energized straight copper wire. The magnetic field generated by the wire can be easily calculated theoretically, allowing for a comparison between the experimental and theoretical results. This verification process enhances the credibility of the magnetic field scanning outcomes for the anti-counterfeiting wire.

In Fig. 4(a), a 10-cm-long and 1.08-mm-diameter copper wire is securely fixed onto an electric displacement table by using an insulating bracket. The fiber optic diamond probe is adjusted to maintain a distance of 120 μm from the wire. The scanning area has dimensions of 3.2 cm×3.2 cm, in scanning steps of 25 μm. The initial frequency for scanning is set to the leftmost peak (2608 MHz) from Fig. 3(b), in a frequency range from 2580 MHz to 2630 MHz.

To generate a stable static magnetic field around the wire, a constant current of 2000 mA is applied to it. Throughout the scanning process, for each completed step of 25 μm by the displacement table, the program calculates the ODMR spectrum for a single peak and performs Lorentz fitting by using Eq. (2). Simultaneously, the program records the frequency value of the symmetry axis of the ODMR.

Figure 4(b) illustrates the position changes of the ODMR relative to the initial ODMR at a specific point in the scanning process. By dividing the frequency difference by the electron spin gyromagnetic ratio γ_{NV}, the magnetic field at each point is determined. The program saves the magnetic field values for each point in a TXT file. After completing the scanning, we input the TXT file into MATLAB for visualization, resulting in the magnetic field distribution image as displayed in Fig. 4(c).

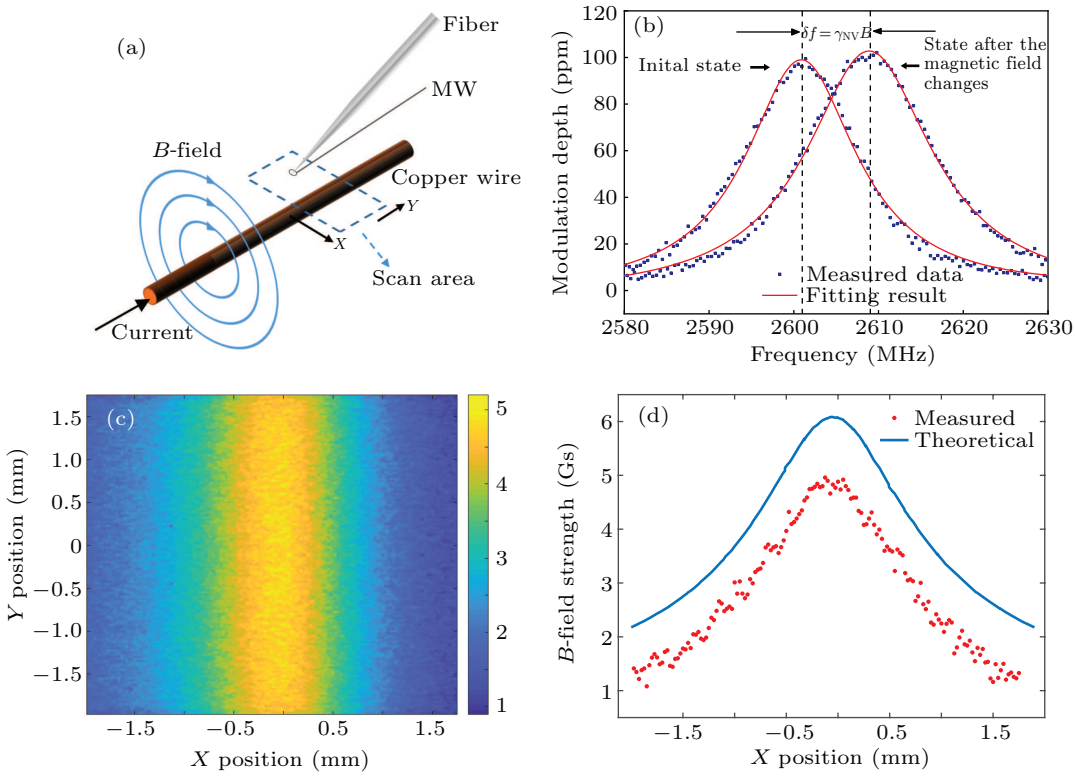


Fig. 4. (a) Schematic diagram of magnetic field scanning setup for energized straight copper wire. (b) Shift in ODMR position during scanning process, with the left peak representing initial state and the right peak denoting state after magnetic field changing. (c) Scanning results of the magnetic field generated by electrified copper wire. (d) Magnetic field distributing along the X direction at $Y = 0$, with solid blue line denoting theoretical value and the red scatter point representing measured value.

To verify whether the scanning results are consistent with the theoretical magnetic field distribution, we calculate the theoretical magnetic field distribution along the X direction at $Y = 0$ mm. According to Biot–Savart law, the magnetic field element $\mathrm{d}\boldsymbol{B}$ generated by a current source of length $\mathrm{d}\boldsymbol{l}$ at distance r can be expressed as

$$\mathrm{d}\boldsymbol{B} = \frac{\mu_0}{4\pi}\frac{I\mathrm{d}\boldsymbol{l}\times\boldsymbol{e}_\mathrm{r}}{r^2}, \tag{3}$$

where $\mu_0 = 4\pi\times10^{-7}$ represents the vacuum permeability and $\boldsymbol{e}_\mathrm{r}$ is the radial unit vector. After performing integration in the Y direction, we obtain the results depicted by the blue curve in Fig. 4(d). The corresponding experimental data are represented by the red dots below the curve. Through comparison, we observe that the experimental results effectively capture the trend of the magnetic field distribution. The discrepancy in values between the experimental data and the integrated curve arises from the fact that we solely measure the magnetic field component along a single NV axis.

The scanning results obtained from the energized straight copper wire demonstrate the accuracy of our method in capturing the magnetic field distribution trend of the tested sample. By following the same experimental procedures and data processing methods, we successfully obtain the magnetic field image of the banknote anti-counterfeiting strip, as presented in Fig. 5(a). The scanning area for this image is 70 μm×125 μm in scanning steps of 12.5 μm.

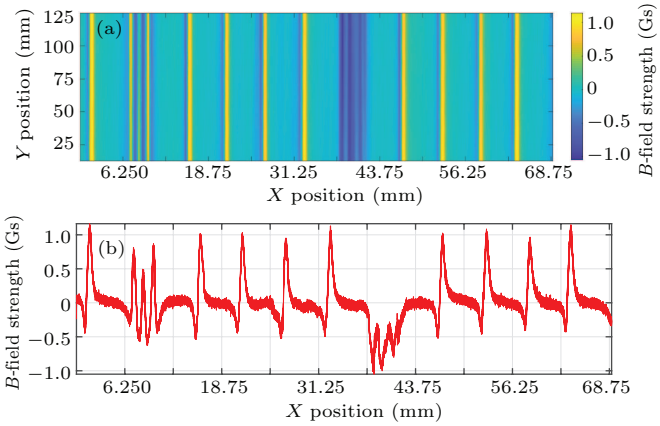


Fig. 5. (a) Results of the magnetic field scanning for banknote anti-counterfeiting strips. (b) The magnetic field distribution along the X axis at $Y = 75$ μm.

From the scanning imaging, it is evident that the magnetic field generated by the anti-counterfeiting strip is on the order of 1 Gs (Gauss) and exhibits a certain periodicity along its overall length. To provide a clearer depiction of the magnetic field magnitude in different regions, we illustrate the magnetic field distribution along the X direction at $Y = 75$ μm in Fig. 5(b). Notably, three distinct types of magnetic field patterns are observed, which we refer to as type A, type B, and type C, respectively.

Type A possesses both positive peaks and negative peaks, while type B appears to be a combination of various type A patterns. Type C, on the other hand, is distinctive in that all

of its peaks have negative values. In the following subsection, we will delve into the underlying reasons for the formation of these three magnetic field patterns.

3.2. Simulation and analysis

In order to gain a deeper understanding of the magnetic field pattern observed in Fig. 5(a) and its relation to the microstructure of the banknote anti-counterfeiting strip, we conduct simulations by using the DC-magnetic-field-module within the COMSOL Multiphysics software. This simulation approach takes into account two crucial aspects: geometric structure and material composition, as they play pivotal roles in determining the magnetic field pattern and its magnitude, respectively.

The geometric structure of the anti-counterfeiting strip is a key factor in generating the observed magnetic field patterns. By analyzing the simulated results, we can gain insights into how specific microstructures in the strip contribute to the magnetic field distribution. Additionally, the material composition of the strip also influences the magnetic field strength. By considering the magnetic properties of different materials and their distributions in the strip, we can understand the variations in the magnetic field values in different regions.

By combining the experimental scanning results with the simulations, we can establish a relationship between the observed magnetic field pattern and the microstructure of the anti-counterfeiting strip. This integrated approach will provide valuable insights into the underlying mechanisms and contribute to a comprehensive understanding of the magnetic field generation process.

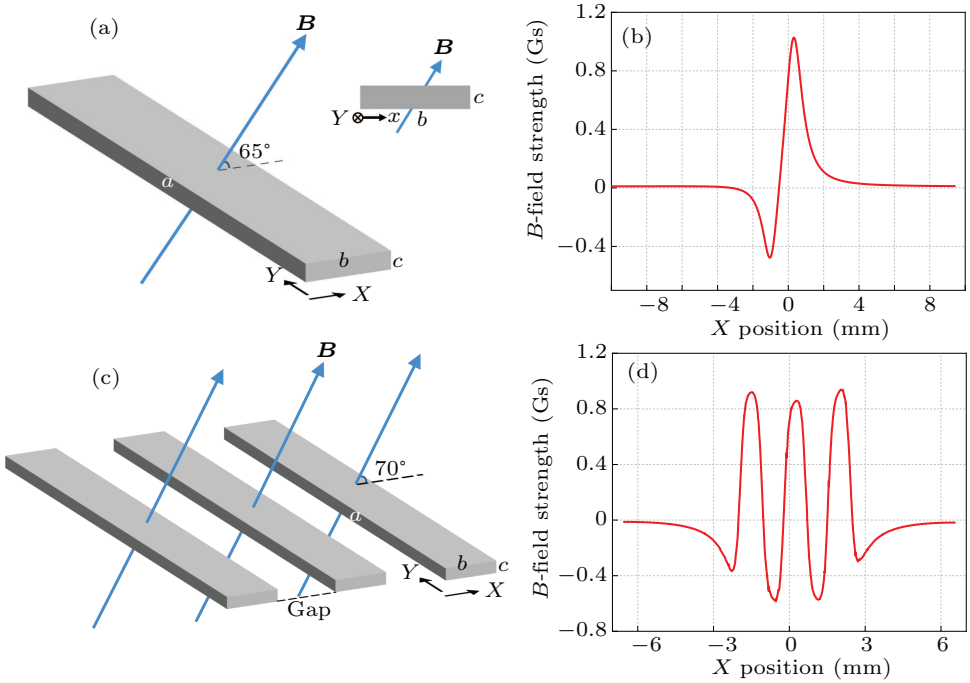


Fig. 6. (a) The structure that generates type-A magnetic field pattern. (b) Simulation result of type-A magnetic field pattern. (c) Structure that generates type-B magnetic field pattern. (d) Simulation results of type-B magnetic field pattern.

For the magnetic field region of type A, we presume that it has the structure in Fig. 6(a), where a represents the width of the anti-counterfeiting stripe, corresponding to the scenario in the Y direction in Fig. 5(a), and the magnetic field in this direction is consistent, so this parameter is not important for the simulation. Parameter b represents the width of the magnetic area in the anti-counterfeiting stripe. Parameter c represents the thickness of the magnetic area, and the blue line arrow denotes the background magnetic field $\boldsymbol{B}$ generated by the permanent magnet. Under the influence of $\boldsymbol{B}$, the banknote anti-counterfeiting strip will be excited to generate an external magnetic field, which is the cause of the patterns in Fig. 5(a). The angle between the $\boldsymbol{B}$ and the magnetic anti-counterfeiting stripe is α. As the size of the magnetic region is at a micron level and the position of the permanent magnet is not changed in the scanning process, the background magnetic field $\boldsymbol{B}$ can be considered to be uniformly isotropic. Thus, there are three adjustable parameters b, c, and α. After continuous trial and adjustment, it is found that the combination of parameters $b = 0.75$ mm, $c = 0.1$ mm, and $\alpha = 65°$ will produce the same shape as the magnetic pattern of type A in Fig. 5(b). The next step is to consider the material in magnetic region to make the magnitude of the magnetic field consistent with the experimental result. From the ODMR spectrum in Fig. 3(b) combined with Eq. (1), we can obtain the background magnetic field $|\boldsymbol{B}|$ of about 100 Gs. Given that the magnetic field generated in the magnetic region is very small, only about 1 Gs, we consider using a ferrite material with a

lower saturation magnetization intensity to make its magnitude of magnetic field closer to the experimental result by adjusting its relative magnetic permeability. Finally, we chose BMHFi-6/23-B with relative permeability $\mu_r = 12$ and obtain the signal waveform shown in Fig. 6(b), which is very close to the experimental result. It is worth noting that we are more concerned with the magnetic field's pattern than the magnitude of magnetic field. In other words, our simulation focuses on the microstructure of the anti-counterfeiting strip rather than its material composition, as other types of materials may also generate magnetic fields of the same value.

For the type-B magnetic pattern, we have taken into account its similarity to type-A and put forth a potential geometric structure as depicted in Fig. 6(c). After conducting tests, we determine that the gap between two adjacent regions should be set to 0.48 mm. By simulating this specific configuration, we can obtain a magnetic signal waveform (Fig. 6(d)) that closely resembles the experimental result of the type-B pattern. Notably, we introduce a magnetic field angle α of 70° at this stage. This adjustment is based on the observation that the magnetic area in the production of the banknote anti-counterfeiting strip may not be perfectly parallel to the banknote surface. Instead, there may be an angle of approximately 5° between the magnetic field at 65° relative to the banknote surface and the material inside the area generating the magnetic signal. Consequently, we set the magnetic field angle α to 70° to account for this discrepancy.

Regarding the type-C magnetic signal, despite various attempts to adjust the size, shape, and magnetic field direction of the magnetic region, we are unable to obtain simulation results consistent with the experimental data. However, interestingly, we discovered that the surface of the banknote corresponding to the type-C magnetic signal is coated with magnetic ink, as depicted by the red semicircle area in Fig. 7(a). We speculated that the irregular magnetic field generated by the magnetization caused by the background magnetic field in this region is superimposed on the magnetic field generated by the magnetic anti-counterfeiting stripe buried beneath the banknote's surface after being magnetized. As a result, a distinct type-C magnetic signal is produced. However, the signal characteristics in this area indicate that if the anti-counterfeiting stripe is unaffected by the magnetic ink, the magnetic pattern it generates should align with the magnetic signal of type B. Figure 7(b) provides an overview of the simulation results, where both types of magnetic signals appear periodically. From these findings, we infer that the banknote's magnetic anti-counterfeiting stripe is a segment intercepted from a longer intact anti-counterfeiting stripe. It is likely that multiple such cycles exist in the intact anti-counterfeiting stripe. Additionally, in different regions of the banknote, the magnetic field strength is uniform. The magnetic field generated by the magnetic region of the security thread is approximately 1 Gs. If the external magnetic field is changed, the magnitude of the magnetic field excited in the security thread may vary, but the overall distribution remains constant. Therefore, we can utilize magnetic field imaging to verify the authenticity of banknotes.

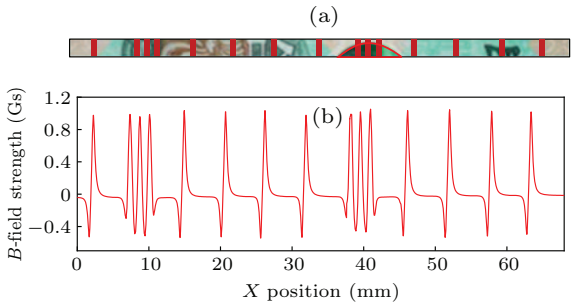


Fig. 7. (a) Physical diagram of magnetic information in red area of RMB 50 denomination anti-counterfeiting stripe. (b) Overall simulation results of magnetic anti-counterfeiting stripe.

4. Conclusions

In this paper, we use a micron optical fiber diamond scanning probe as a magnetic field sensor to conduct high-resolution scanning of the 50-yuan RMB anti-counterfeiting stripe, and obtain detailed imaging of the magnetic field distribution. According to these experimental findings, we further utilize finite element software to perform simulations, aiming at inferring the potential magnetic structures in the banknote anti-counterfeiting stripe. Through iterative adjustments of simulation parameters, we progressively achieve closer alignment between the simulation results and the experimental data. Our work presents a valuable approach to the direct and quantitative characterization of weak magnetic signals. The methods and concepts proposed in this paper can be readily applied to other banknotes or similar samples requiring testing. The research results can be used as information feedback to promote the development of banknote anti-counterfeiting technology.

Acknowledgements

Project supported by the National Key Research and Development Program of China (Grant No. 2021YFB2012600) and the Shanghai Aerospace Science and Technology Innovation Fund, China (Grant No. SAST-2022-102).

References

[1] Yuan W Q and Li Z Q 2015 *Electronic Design Engineering.* **23** 110 (in Chinese)
[2] Weiss B P, Lima E A, Fong L E and Baudenbacher F J 2007 *Journal of Geophysical Research: Solid Earth* **112** B9
[3] Wang M S, Kang L X, Su J W, Zhang L M, Dai H W, Cheng H, Han X T, Zhai T Y, Liu Z and Han J B 2020 *Nanoscale* **12** 16427
[4] Serri M, Cucinotta G, Poggini L, Serrano G, Sainctavit P, Strychalska-Nowak J, Politano A, Bonaccorso F, Caneschi A, Cava R J, Sessoli R, Ottaviano L, Klimczuk T, Pellegrini V and Mannini M 2020 *Adv. Mater.* **32** 2000566

[5] Uehara M and Nakamura N 2007 *Rev Sci Instrum.* **78** 043708

[6] Doherty M W, Manson N B, Delaney P, Jelezko F, Wrachtrup J and Hollenberg L C 2013 *Phys. Rep.* **528** 1

[7] Gruber A, Drabenstedt A, Tietz C, Fleury L, Wrachtrup J and Borczyskowski C V 1997 *Science* **276** 2012

[8] Yang B, Dong M M, He W H, Liu Y, Feng C M, Wang Y J and Du G X 2019 *IEEE T. Microw. Theory* **67** 2451

[9] Yin X H, Liu X Y, Gu B X, Zhang J J, Li X C and Du G X 2021 *Int. J. RF Microw. Comput. Aided Eng.* **32** 23036

[10] Rondin L, Tetienne J P, Hingant T, Roch J F, Maletinsky P and Jacques V 2014 *Rep. Prog. Phys.* **77** 056503

[11] Schirhagl R, Chang K, Loretz M and Degen C L 2014 *Rev. Phys. Chem.* **65** 83

[12] Casola F, Van Der Sar T and Yacoby A 2018 *Nat. Rev. Mater.* **3** 17088

[13] Taylor J M, Cappellaro P, Childress L, Jiang L, Budker D, Hemmer P R, Yacoby A, Walsworth R and Lukin M D 2008 *Nat. Phys.* **4** 810

[14] Fu R R, Weiss B P, Lima E A, Harrison R J, Bai X N, Desch S J, Ebel D S, Suavet C, Wang H P, Glenn D, Sage D L, Kasama T, Walsworth R L and Kuan A T 2014 *Science* **346** 1089

[15] Farchi E, Ebert Y, Farfurnik D, Haim G, Shaar R and Bar-Gill N 2017 *Spin* **7** 1740015

[16] Glenn D R, Lee K, Park H, Weissleder R, Yacoby A, Lukin M D, Lee H, Walsworth R L and Connolly C B 2015 *Nat. Methods* **12** 736

[17] Le Sage D, Arai K, Glenn D R, DeVience S J, Pham L M, Rahn-Lee L, Lukin M D, Yacoby A, Komeili A and Walsworth R L 2013 *Nature* **496** 486

[18] Gould M, Barbour R J, Thomas N, Arami H, Krishnan K M and Fu K M C 2014 *Appl. Phys. Lett.* **105** 072406

[19] Shao L B, Zhang M, Markham M, Edmonds A M and Lončar M 2016 *Phys. Rev. Appl.* **6** 064008

[20] Horsley A, Appel P, Wolters J, Achard J, Tallaire A, Maletinsky P and Treutlein P 2018 *Phys. Rev. Appl.* **10** 044039

[21] Goldman M L, Doherty M W, Sipahigil A, Yao N Y, Bennett S D, Manson N B, Kubanek A and Lukin M D 2017 *Phys. Rev. B* **91** 165201

[22] Gruber A, Drabenstedt A, Tietz C, Fleury L, Wrachtrup J and Borczyskowski C V 1997 *Science* **276** 2012

[23] Doherty M W, Dolde F, Fedder H, Jelezko F, Wrachtrup J, Manson N B and Hollenberg L C L 2012 *Phys. Rev. B* **85** 205203

[24] Levine E V, Turner M J, Kehayias P, Hart C A, Langellier N, Trubko R, Glenn D R, Fu R R and Walsworth R L 2019 *Nanophotonics* **8** 1945

[25] Bai R X, Yang F, Liu P, Gao T R, Zhou L, Yin, X H, Zhu X Y, Ma W H, He F Y, Chen N C, Sun Y, Ma J T, Yu T and Du G X 2022 *Appl. Phys. Lett.* **120** 044003

[26] Dong M M, Hu Z Z, Liu Y, Yang B, Wang Y J and Du G X 2018 *Appl. Phys. Lett.* **113** 131105

[27] Duan D, Du G X, Kavatamane V K, Arumugam S, Tzeng Y K, Chang H C and Balasubramanian G 2019 *Opt. Express* **27** 6734